

Chains of magnetosomes with controlled endotoxin release and partial tumor occupation induce full destruction of intracranial U87-Luc glioma in mice under the application of an alternating magnetic field

Edouard Alphandéry, Ahmed Idbaih, Clovis Adam, Jean-Yves Delattre, Charlotte Schmitt, François Guyot, Imène Chebbi

▶ **To cite this version:**

Edouard Alphandéry, Ahmed Idbaih, Clovis Adam, Jean-Yves Delattre, Charlotte Schmitt, et al.. Chains of magnetosomes with controlled endotoxin release and partial tumor occupation induce full destruction of intracranial U87-Luc glioma in mice under the application of an alternating magnetic field. Journal of Controlled Release, 2017, 10.1016/j.jconrel.2017.07.020 . hal-01565231

HAL Id: hal-01565231

https://hal.sorbonne-universite.fr/hal-01565231

Submitted on 19 Jul 2017

HAL is a multi-disciplinary open access archive for the deposit and dissemination of scientific research documents, whether they are published or not. The documents may come from teaching and research institutions in France or abroad, or from public or private research centers.

L'archive ouverte pluridisciplinaire **HAL**, est destinée au dépôt et à la diffusion de documents scientifiques de niveau recherche, publiés ou non, émanant des établissements d'enseignement et de recherche français ou étrangers, des laboratoires publics ou privés.

Chains of magnetosomes with controlled endotoxin release and partial tumor occupation induce full destruction of intracranial U87-Luc glioma in mice under the application of an alternating magnetic field.

Edouard Alphandéry [a,b,*], *Ahmed Idbaih* [c], *Clovis Adam* [d], *Jean-Yves Delattre* [c], *Charlotte Schmitt* [c], *François Guyot* [a], *Imène Chebbi* [b].

[a] Institut de minéralogie, de physique des matériaux et de cosmochimie, UMR 7590 CNRS, Sorbonne Universités, UPMC, University Paris 06, Muséum National d'Histoire Naturelle, 4 Place Jussieu, 75005, Paris, France.

[b] Nanobacterie SARL, 36 boulevard Flandrin, 75016, Paris, France.

[c] Inserm U 1127, CNRS UMR 7225, Sorbonne Universités, UPMC, University Paris 06, UMR S 1127, Institut du Cerveau et de la Moelle épinière, ICM, F-75013, Paris, France.
AP-HP, Hôpitaux Universitaires Pitié Salpêtrière - Charles Foix, Service de Neurologie 2-Mazarin, F-75013, Paris, France.

[d] Laboratoire de neuropathologie, GHU Paris-Sud-Hôpital Bicêtre, 78 rue du Général Leclerc, 94270 Le Kremlin Bicêtre, France.

*Corresponding author Email address:

edouardalphandery@hotmail.com

ABSTRACT

Previous studies have shown that magnetic hyperthermia could efficiently destroy tumors both preclinically and clinically, especially glioma. However, antitumor efficacy remained suboptimal and therefore required further improvements. Here, we introduce a new type of nanoparticle synthesized by magnetotactic bacteria called magnetosomes with improved properties compared with commonly used chemically synthesized nanoparticles. Indeed, mice bearing intracranial U87-Luc glioma tumors injected with 13 µg of nanoparticles per mm^3 of tumor followed by 12 to 15 of 30 minutes alternating magnetic field application displayed either full tumor disappearance (40% of mice) or no tumor regression using magnetosomes or chemically synthesized nanoparticles, respectively. Magnetosome superior antitumor activity could be explained both by the increased production of heat and by endotoxin release under the alternating magnetic field application. Most interestingly, this behavior was observed when magnetosomes occupied only 10% of the tumor volume, which suggests that an indirect mechanism, such as an immune activity, is involved in tumor regression. This is desired for the treatment of infiltrating tumors, such as glioma, for which whole tumor coverage by nanoparticles can hardly be achieved.

KEYWORDS

Magnetosomes, magnetotactic bacteria, magnetic hyperthermia, alternating magnetic field, glioblastoma.

1. INTRODUCTION

A series of different nanotechnologies, such as lipid-based nanoformulations, polymer-drug conjugates, recombinant viruses, metallic nanoparticles, drug-targeted antibodies, and herbal nanoparticles, have been successfully developed for cancer treatment both at fundamental and industrial levels (1). Among them, technologies in which nanoparticle anti-tumor activity can be controlled by applying an external source of energy, such as a laser (2), (3), radiation (4), (5), ultrasound (6), (7), or magnetic field (8), (9) appear promising because they can potentially enhance both treatment safety and efficacy. Strategies to increase nanoparticle SAR by combining magnetic hyperthermia with photothermia using magneto-plasmonic nanohybrids have also been suggested (10), (11). There is interest in developing this type of nanotechnology for glioblastoma (GBM) treatment, especially for the most severe GBM cases, which are non-operable. With the current standard of care, *i.e.,* maximal safe surgery, concurrent radiochemotherapy and adjuvant chemotherapy, GBM, which affects 25,000 patients per year in the United States and Europe (12), (13), remains incurable with a poor prognosis. The five-year survival time of patients with GBM is low at 10% (14), (15), demonstrating the need for new treatment options (16), (17), (18), (19), (20). Among the potential treatments for GBM are different types of nanothermotherapies (21), such as photodynamic therapy (22) and magnetic hyperthermia, which have been tested to treat GBM (9). Compared with other thermotherapies, magnetic hyperthermia (23), (24), (25), (26), (27), in which tumors are typically heated to 43-50 °C by intratumor administration of iron oxide nanoparticles followed by alternating magnetic field (AMF) application, appears promising. This is due to more localized heat produced by the nanoparticles, which results in enhanced efficacy, and to tumor destruction achieved at lower temperatures, which strengthens treatment safety. In a clinical trial that enrolled 14 patients with GBM, magnetic hyperthermia treatment performed using small chemically synthesized iron oxide nanoparticles (IONP) was well-tolerated by

patients, did not produce major side effects, and led to an increased survival time of 7 months compared with conventional treatments (28), (29).

Treatment efficacy could potentially be further improved by using chains of magnetosomes (CM), which are iron oxide nanoparticles synthesized by magnetotactic bacteria, instead of IONP. In previous studies, CMs have been shown to destroy MDA-MB-231 breast tumors subcutaneously xenografted under the skin of mice more efficiently than IONPs (30), (31). Magnetosome efficacy was attributed to the large magnetosome size, leading to stable ferrimagnetic properties and to a large amount of heat produced under AMF application, as well as to an arrangement of chains that prevented aggregation and promoted homogenous magnetosome distribution in the tumor (32), (33), (34), (35).

In the present study, anti-tumor activity against U-87-Luc GBM was studied both *in vitro* and *in vivo* with a suspension containing CMs. We first demonstrated that the amount of endotoxins released from the CMs can be controlled under AMF applications. CM cytotoxicity and internalization properties in the presence of U87-Luc cells were also studied *in vitro*. Mice bearing intracranial U87-Luc tumors were then treated under conditions that could be followed clinically, *i.e.,* using an AMF with 30 mT and 198 kHz ($H.f = 8\ 10^8\ A.m^{-1}.s^{-1}$, below the threshold of $5.10^9\ A.m^{-1}.s^{-1}$, above which Eddy currents may occur) (26),(36). Treatment parameters, such as the number of magnetic sessions and quantity of CMs administered, that lead to complete disappearance of the intracranial U87-Luc tumors were determined and compared with IONP treatment, which has been previously used to perform preclinical magnetic hyperthermia tumor treatments (37), (38). During the various treatments, nanoparticle distribution in the tumors and the presence of different cell types in the brain were also examined by histology. This study also suggests a mechanism for tumor destruction and verified that the brain tumor disappeared fully following magnetic hyperthermia treatment with CMs.

2. MATERIALS AND METHODS

2.1. Preparation of the injectable CM suspension

Magnetospirillum magneticum AMB-1 magnetotactic bacteria at biosafety level 1 were purchased from ATCC (79024 strain). Five milliliters of a suspension containing 4.10^6 of these bacteria per milliliter were introduced into one liter of sterile 1653 ATCC culture medium containing nutrients and additives, such as minerals, vitamins, and an iron source, as listed in the 1653 ATCC medium, which is required for the proliferation of these bacteria and for magnetosome production. The bottles were completely filled with sterile medium to prevent contamination by other bacterial species and to avoid a high oxygen concentration in the growth medium, which would prevent magnetosome production. The media containing the bacteria were then placed in an incubator at 30 °C for 7 days to enable bacterial growth and magnetosome production. After 7 days, the media was centrifuged at 4000 g for 45 minutes. The bacterial pellet was washed using 1 ml of sterile water (Millipore®). Magnetotactic bacteria were concentrated using a strong Neodinium magnet (0.6 Tesla), re-suspended in 0.05 M TRIS and sonicated with a sonicating finger at 0 °C for 2 hours at 30 W. The suspension containing the chains of magnetosomes extracted from the magnetotactic bacteria was washed several times with sterile water using a magnet to isolate the CMs from the supernatant containing cellular debris and residual bacteria until the cellular debris disappeared from the supernatant. Sonication was performed at 30 W by a series of three 2-second pulses between each wash. The CMs were then re-suspended in 1 ml of sterile water. For the intracranial injections, the CMs were re-suspended in a sterile injectable solution containing 5% glucose and exposed to ultraviolet lamp (UV) irradiation for 12 h for partial sterilization.

2.2. Preparation of IONPs:

IONPs, which are starch-coated iron oxide nanoparticles, were purchased from Micromod Partikeltechnologie GmbH company, Friedrich-Barnewitz-Str. 4, D-18119, Rostock, Germany (ref: 10-00-102).

2.3. Nanoparticle Characterization:

Nanoparticle sizes, shapes, and organization were determined using a transmission electron microscope (JEM-2100, JEOL, Japan). The iron concentrations of the different nanoparticle suspensions were measured by mixing these suspensions with hydrochloric acid and hydrogen peroxide to produce Fe^{3+}

ions complexed with potassium thiocyanate, and total iron was then determined via an absorbance measurement at 476 nm. The concentrations were expressed as mg of maghemite contained in the CMs and IONPs per ml of suspension or per mm^3 of tumor. The zeta potentials of the different nanoparticles in suspension were measured by dynamic light scattering (DLS, ZEN 3600, Malvern Instruments, UK). The stability of the nanoparticle suspensions was estimated by measuring the changes in the optical densities of these suspensions, which were measured at 476 nm for 15 min. Nanoparticle FTIR spectra were recorded with a FTIR spectrometer (Vertex 70, Bruker, USA). The amount of organic material at the nanoparticle surface was measured using an elemental CHNS analyzer (Flash EA 1112, Thermo Fisher Scientific, USA). More details about each of these techniques are provided in the supplementary materials section.

2.4. Set-up for generating the alternating magnetic field and for measuring the temperature

We used an induction system operating at 198 kHz to generate the alternating magnetic field. Mice, Eppendorf tubes, petri dishes containing nanoparticles and possibly cells were inserted into a coil with a 7-cm diameter with four spires to generate a magnetic field with an average strength of 30 mT. We used an infrared camera (EasIR-2, Optophase, France) positioned 20 cm above the coil to measure the temperature both *in vitro* and *in vivo*. We verified the temperature with a thermocouple positioned at the tumor center and that the infrared camera measured the temperature at the tumor center. This was possible due to the shallowness of the tumor.

2.5. Amount of endotoxins released under AMF application

Suspensions containing 2 µl of CMs or IONPs at a concentration of 20 mg/ml in iron oxide were treated as follows. Nanoparticle suspensions were exposed to 0, 1, 2, 3, and 4 magnetic sessions, during which an AMF of 198 kHz and average strength of 30 mT was applied for 30 minutes. After AMF applications, 100 µl of nonpyrogenic water was added to the suspensions, and the suspensions were mixed for one minute and centrifuged at 13 000 rotations per minute for 15 minutes. The endotoxin concentration of the supernatant was measured using the Limulus amebocyte lysate (LAL) assay.

2.6. Materials and cells culture

U87-MG Luc human GBM cell lines, which were transduced with a luciferase gene, were obtained from Keith Ligon's lab and used in this study. After thawing, the U87-MG Luc adherent cells were cultivated at 37 °C in the presence of 5% CO_2 in Dulbecco's Modified Eagle Medium (DMEM) containing 10% fetal bovine serum (FBS). Once the cells reached confluence, the culture dishes were rinsed with Hank's Balanced Salt Solution (HBSS). The cells were then detached with trypsinization for 5 minutes at 37 °C in the presence of 5% CO_2. The trypsin activity was stopped by the addition of medium containing FBS. The cellular concentration was then determined using a Malassez cell.

2.7. U87-Luc cytotoxicity in the absence of AMF using an MTT assay

U87-Luc cytotoxicity studies were evaluated using an MTT assay. This technique measures the ability of mitochondrial enzymes to reduce 3-(4,5-dimethylthiazol-2-yl)-2,5-diphenyltetrazolium bromide to purple formazan crystals. Cells were seeded at a density of 10^4 cells per well in 96-well flat-bottom plates and incubated in completed culture medium for 24 h. Then, the U87-Luc cell medium was removed and replaced with 10% FCS-medium containing CMs or IONPs at varying concentrations ranging from 7.8 µg/ml to 1000 µg/ml in maghemite. After 24 h of incubation, the cells were washed with HBSS and incubated with 0.1 ml of MTT (2 mg/ml) for an additional 4 h at 37 °C. The insoluble product was then dissolved by the addition of 100 ml of isopropanol. The absorbance corresponding to the solubilized formazan pellets, which reflect the relative viable cell numbers, was measured at 540 nm using a microplate reader. We measured the absorbance at 540 nm for the cells with the nanoparticles without formazan blue and we have subtracted this signal from the signal for the cells with nanoparticles with formazan blue. The percent inhibition of cell proliferation, inhibition (%), was then estimated using the following formula: % inhibition = $[1-(OD_{TC}/OD_{UC})] \times 100$, where OD_{UC} is the optical density of the suspension of untreated cell, *i.e.,* cells that have been washed with PBS and have not been in the presence of nanoparticles, measured at 540 nm, and OD_{TC} is the optical density of the suspension of treated cells, *i.e.,* nanoparticle suspensions that have been added to cells, measured at 540 nm. The percent inhibition of cell proliferation was plotted as a function of the nanoparticle concentration. The experiments were performed in triplicate.

2.8. In vitro efficacy of hyperthermia

A total of 500,000 U87-Luc cells were seeded in a Petri dish (35 mm) for 24 hours. Then, 2 ml of IONP and CM suspensions were added to the cells at different concentrations varying between 1 mg/ml, which is sufficient to induce an increase in temperature increase, and 40 µg/ml, which corresponds to the maximum magnetosome concentration in the tumor, *i.e.*, 40 µg of magnetosomes per mm^3 of tumor. When the same amount of nanoparticles used, we observed an increase in the temperature in solution but not *in vitro*, possibly due to the lower concentrations *in vitro* (2 ml at 20 µg/ml) than in solution (2 µl at 20 mg/ml). Next, these assemblies were exposed (or not) to a 30 mT and 198 kHz AMF for 30 minutes. The cells were then incubated with the nanoparticles for 24 h. The nanoparticle media was removed, and the cells were washed twice with cold PBS. We verified that there were no observable nanoparticle aggregates at the cell surface and that the nanoparticles were mostly internalized in cells by optical microcopy. It is possible that nanoparticles that were not observed with the optical microscope remained at cell surface, meaning that the measurement provides an estimate of the maximum quantity of internalized nanoparticles or the amount of nanoparticles internalized in cells or at the cell surface. Next, 250 µl of trypsin were added to detach the cells, and then the culture media was mixed with cells. Following this *in vitro* treatment, the mixtures were centrifuged at 800 rpm for 7 minutes. The supernatant was removed and replaced with 100 µl of annexin-binding buffer, 5 µl of Alexa Fluor 488 Annexin V for early apoptosis detection, and 1 µl of propidium iodide at 100 µg/ml for late apoptosis and necrosis detection. The mixtures were incubated at room temperature for 15 minutes. Then, 400 µl of annexin-binding buffer was added to this cell suspension and mixed gently. Ten microliters of this suspension were loaded into the sample slide and were inserted completely into a Countess™ II FL Automated Cell Counter (Thermo Fisher scientific), which was able to detect the Annexin and Propidium Iodide emissions. The percentages of necrotic and apoptotic cells were thus obtained.

2.9. Internalization of nanoparticles

Following the *in vitro* treatments described in 2.7, the different mixtures were loaded into the sample slide and completely inserted into a Countess™ II FL Automated Cell Counter to count the cells. The

198 mixtures were then centrifuged, and the supernatant was removed and replaced with 286 µl of HNO_3
199 (70%); the resulting treated mixtures were maintained at 4 °C for 24 h to lyse cells and dissolve the
200 nanoparticles into free iron. Finally, 10 ml of filtered water was added to all the treated mixtures and the
201 iron concentration was then determined using ICP-AES measurements. We deduced the average
202 quantity of iron coming from the nanoparticles, which was internalized in each cell.

203 ***2.10. In vivo experiments***

204 *In vivo* experiments were performed following ethical guidelines and surgery was performed following
205 the guidelines of the Institutional Animal Care and Use Committee ("Ethic committee Charles Darwin
206 N°5", project ethic number: 00764.03). Mice were fed and watered according to these guidelines and
207 euthanized by cervical dislocation when their weights had decreased by more than 20% or when signs of
208 pain, unusual posture or prostration were observed. At day 0 (D0), a cell suspension containing 10^5 U87-
209 Luc cells per microliter was first inoculated into the brains of 7-week-old CD-1 female nude mice with a
210 mean weight of 20 g from Charles River. To achieve the surgical procedure leading to cell implantation,
211 the mice were first anesthetized with a mixture of ketamine (100 mg/kg) and xylazine (8 mg/kg). The
212 mouse head was then fixed in a stereotactic frame, a craniotomy was performed at the fixed coordinates
213 (0.2.0) and 2 µl of a suspension containing 2.10^5 U87-Luc cells were injected at the coordinates (0.2.2).
214 Tumors grew for 8 days between D0 and D8. At D8, 7 different groups containing 10 mice each were
215 treated as follows (Table S1(a)):

216 - Group 1 received a 30 mm^3 GBM at coordinates (0.2.2) mm and 2 µl of an isotonic solution
217 containing 5% glucose without any further treatment;

218 - Group 2 received a 5 mm^3 GBM at coordinates (0.2.2) mm and the same glucose solution as
219 Group 1, followed by magnetic treatment consisting in 12 magnetic sessions (S) on D8 (S1), D9 (S2),
220 D10 (S3), D15 (S4), D16 (S5), D17 (S6), D22 (S7), D23 (S8), D24 (S9), D29 (S10), D30 (S11), and
221 D31 (S12);

222 - Group 3 received a 3 mm^3 GBM at coordinates (0.2.2) mm and a suspension containing 40 µg of
223 magnetosome chains in maghemite without any further treatment;

- Group 4 received a 3 mm^3 GBM at coordinates (0.2.2) mm and the same suspension as Group 3, followed by magnetic treatment consisting in 15 magnetic sessions on D8 (S1), D9 (S2), D10 (S3), D15 (S4), D16 (S5), D17 (S6), D22 (S7), D23 (S8), D24 (S9), D29 (S10), D30 (S11), D31 (S12), D36 (S13), D37 (S14), and D38 (S15);
- Group 5 received a 25 mm^3 GBM at coordinates (0.2.2) mm and the same suspension as group 3, followed by 15 magnetic sessions on D8 (S1), D9 (S2), D10 (S3), D15 (S4), D16 (S5), D17 (S6), D22 (S7), D23 (S8), D24 (S9), D29 (S10), D30 (S11), D31 (S12), D36 (S13), D37 (S14), and D38 (S15);
- Group 6 received a 5 mm^3 GBM at coordinates (0.2.2) mm and 40 µg of IONPs in maghemite without any further treatment; and
- Group 7 received in a 3 mm^3 GBM at coordinates (0.2.2) mm and the same suspension as Group 6, followed by 12 magnetic sessions on D8 (S1), D9 (S2), D10 (S3), D15 (S4), D16 (S5), D17 (S6), D22 (S7), D23 (S8), D24 (S9), D29 (S10), D30 (S11), and D31 (S12).

For the different groups of mice, the bioluminescence intensity emitted by the living tumor cells was measured on D7, D14, D21, D28, D35, D42, D49, D56 and D150.

During each magnetic session (S1 to S15), the mice were exposed to an AMF at an average strength of 30 mT and a frequency of 198 kHz that was applied for 30 minutes.

2.11. Bioluminescence intensity and tumor volume measurements

The mice were first anesthetized using isoflurane. The bioluminescence intensity was then measured using an IVIS Spectrum *"In Vivo Imaging System"* (PerkinElmer, Inc.) 10 minutes after intraperitoneal injection of 100 mg/kg of beetle luciferin potassium salt (Promega: E1605) in PBS, which reacts with luciferase to produce luminescent oxo-luciferin, (39), (40), (41). Images were analyzed with the living Image 4.0 software from Caliper, Life Sciences. The bioluminescence intensity at the tumor site was divided by the bioluminescence intensity measured in the flanks to remove the mouse auto-luminescence signal. Then, the relationship between tumor bioluminescence intensity and tumor volume was determined. For that, bioluminescence intensities were measured at D7, D14, D21, D28 and D35 in a series of living mice. The tumor volumes were deduced from surface measurements of several

horizontal histological sections positioned at various tumor heights, which were collected from mice euthanized on the same day at the BLI measurements. A linear relationship was observed between the logarithm of tumor bioluminescence intensity (BLI), log(BLI), and the logarithm of the tumor volume expressed in mm^3, log (volume(mm^3))(Fig. S3). A linear coefficient of 1.4 was deduced by fitting the plot in Fig. S3 with a linear function, a value that agrees with previously reported values (40), (42), (43), (44).

2.12. Representation of tumor volume variations and estimates of survival time

The variations in tumor volume in time were represented in Tukey diagrams using the Kaleida Graph 4.03 software. Mouse survival times are plotted using the Kaplan-Meier model method (45), (46). The statistical significance of the survival time between the different groups was evaluated using the log rank test. Parameters are expressed as the median with p-values (9).

2.13. Temperature measurements

Intratumor temperatures were measured as a function of time during the various treatments in living mice using an infrared camera (EasIRTM^{-2}, Optophase) placed 20 cm above the coil.

2.14. Histological analysis

Histological studies were performed on extracted brains that were fixed with a 4% solution of formaldehyde for 24 hours, cut into 2-mm thickness transverse slices, washed in an ethanol (70%) bath for 12 hours and included in paraffin. Sections of paraffin blocks with a thickness of 4 µm were deposited on glass slides and stained with hematoxylin-eosin (H&E) and/or Prussian blue to distinguish between healthy and tumor areas and to determine the location of the magnetosomes, polynuclear neutrophils (PNN), and tumor and healthy cells. Histological analysis was also performed on the mice that received glucose on day 8 and were euthanized 6 or 24 hours following glucose injection (Figs. S5(a) and S5(c)). Six mice were analyzed at various times, including after 1 magnetic session (Figs. S5(b)) or 24 hours after 3 magnetic sessions (Fig. S5(d)), in which they received CM on day 8 and were euthanized 4 hours (Figs. 9(a) and 9(c)) or 72 hours (Figs. 9(b) and 9(d)) after the CM injection; just after or 4 hours after 1 magnetic session (Figs. 8(a), 8(b) and 8(c)); and 24 hours after 3 magnetic

sessions (=72 hours, Figs. 8(d) to 8(g)), in which they received IONPs on day 8 and were euthanized 6 or 72 hours after IONP administration (Figs. S4(a) and S4(c)) or 24 hours after 3 magnetic sessions (72 hours (Figs. S4(b) and S4(d)).

3. RESULTS AND DISCUSSION

3.1. Properties of CMs and IONPs used for the tumor magnetic hyperthermia treatments

CMs were extracted from AMB-1 whole magnetotactic bacteria, a species of bacteria that produces chains of nanoparticles called magnetosomes, as shown in the TEM image of a typical magnetotactic bacterium presented in Figure 1(a). After extraction from the magnetotactic bacteria, the magnetosomes maintain their organization in chains (Figure 1(b)), a type of organization that is advantageous for the treatment because it prevents aggregation and promotes uniform distribution and homogenous heat production. Magnetosomes appear to possess a cubooctahedric geometry, more uniform sizes and shapes than IONPs (Figs. S7(a) and S7(b)), a size that is larger than 20 nm for the majority of them and a mean size of ~45 nm (Fig. S1(a)), which leads to a coercivity H_c of ~200-300 Oe and a ratio between remnants and saturating magnetization of Mr/Ms ~ 0.35 at physiological temperature (Fig. S6), (47).

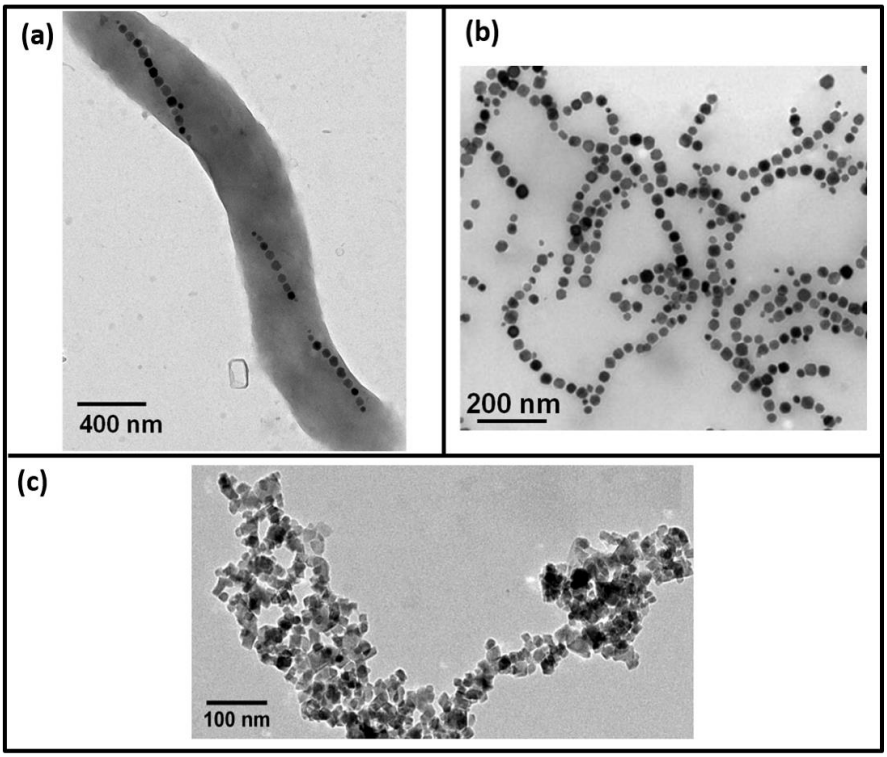


Figure 1: Transmission electron microscopy images of (a) an AMB-1 *Magnetospirillum magnetotacticum* magnetotactic bacterium, (b), chains of magnetosomes extracted from magnetotactic bacteria and (c) an IONP. Seven microliter suspensions containing magnetotactic bacteria, chains of magnetosomes, and IONPs were deposited and dried on top of a carbon grid before TEM observation.

Magnetosomes are composed of a core, which is made of iron oxide, as revealed by the FT-IR Fe-O peak at 580 cm^{-1} (table 1) and further determined to be maghemite by saturating isothermal remnant magnetic measurements (47). The core is surrounded by a coating of organic material, including phospholipids and lipopolysaccharides, as revealed by a series of FT-IR peaks [C=O at 1740 cm^{-1}, amide at 1650 cm^{-1}, amine at 1530 cm^{-1}, P=O at 1250 cm^{-1}, and PO at 1050 cm^{-1} (Table 1)]. The coating, whose function is to bind magnetosomes together in chains (48), is estimated to be 1 to 5 nm thick (Figure 1(b)) and to contain 13.9% carbon, as estimated by CHNS analysis. LAL measurements further indicated that the organic material at the magnetosome surface is partially derived from endotoxins whose concentration in CM suspensions is estimated as 1400-8400 EU per ml per mg of iron oxide. Moreover, CM suspensions appear sufficiently stable to enable their *in vivo* administration, as their absorption measured at 480 nm does not decrease by more than 30% within 20 minutes (Table 1).

	CM						IONP					
Endotoxin level **(EU/mg/mL)**	1400-8400						< 50					
% stability on water (iron concentration = 1mg/mL)	70						100					
Coating thickness **(nm)**	1 - 5						1					
Isoelectric Point **(a.u)**	4.2						9.5					
pH	2	4	6	8	10	12	2	4	6	8	10	12
ζ-Potential **(mV)**	20	2.5	-18	- 26	-34	- 38	7	6	6	5	3	- 20
% C	13.9						8.7					
SAR (2µL, 40 µg of iron) **(W/gFe)**	Water			Brain			Water			Brain		
	57			4			10			0		
FT-IR **(cm^{-1})**	580	1050	1250	1530	1650	1740	610		1025		1150	
	Fe-O	P-O	P=O	N-H (amine)	N-H (amide)	C=O	Fe-O		C-O (alcohol)		C-O (ether)	

Table 1: The endotoxin content estimated in Endotoxin units (EU per mg in iron per ml), percent decreased absorption measured at 480 nm in suspensions containing CM and IONP at a concentration of 1 mg in iron per ml after twenty minutes, and estimates of the isoelectric point and zeta potential as a function of pH for suspensions containing CMs or IONPs.

Estimates of the coating thickness measured by transmission electron microscopy and percentage of carbon (% C) measured with CHNS and assignments from the different FT-IR peaks measured by FT-IR for the CM and IONP dried suspensions. Estimates of the specific absorption rates (SAR) in W per gram in iron for 2 µl containing 40 µg of CMs or IONPs in iron oxide mixed in water or introduced inside the mouse brains.

Compared with CMs, IONPs are also ferromagnetic iron oxide nanoparticles but characterized by the following distinct features. Their geometric structure is parallelepipedic, they are not organized in chains and tend to form small aggregates as observed in the TEM image in Figure 1(c). INOPs are made of a core measuring ~19 nm by TEM (49), and whose composition is iron oxide as determined by FT-IR measurements that display an Fe-O peak at 610 cm^{-1} (Table 1). The IONP core is surrounded by synthetic hydroxyethyl starch, as suggested by FT-IR and CHNS measurements performed on the IONPs, which shows FT-IR peaks at 1150 cm^{-1} and 1050 cm^{-1} that are attributed to hydroxyethyl starch ether and alcohol functional groups, and has a carbon percent of 8.7%, revealing the presence of an organic coating surrounding the inorganic iron oxide core (Table 1). Compared with CMs, the IONP surface contains a much lower endotoxin concentration of 50 EU per ml per mg of iron oxide, as measured with the LAL assay. Furthermore, IONPs are characterized by ferrimagnetic properties at physiological temperatures but at the following lower values: (1) $H_c \sim 120$ Oe and (2) $M_r/M_s \sim 0.15$ (49), (Fig. S6 and Table 1), which should yield lower SAR values. Furthermore, given that they are not less stable than CMs (Table 1) and that their anti-tumor efficacy has been demonstrated on tumor-bearing mice using magnetic hyperthermia (50), IONPs appear to be good standard for comparison to assess CM efficacy.

3.2. Under AMF applications, CM can release heat and an immune-stimulating substance more efficiently than IONPs

In an attempt to mimic the conditions in the *in vivo* treatments and to study the release of endotoxins from the CM and IONP surfaces in these conditions, we introduced 2 µl of suspensions containing 40 µg of these nanoparticles in iron oxide at the bottom of a tube that we exposed to 1, 2, 3, and 4 magnetic sessions during which an AMF of 198 kHz and average strength 30 mT was applied for 30 minutes. During each of these 4 magnetic sessions, CM and IONP suspensions led to maximal temperatures

(T_{max}) of 57 °C and 28 °C, respectively, after 3 minutes of AMF application (Fig. S2(a)). Specific absorption rates (SAR) were deduced from the formula $SAR=C_{water}(\Delta T/\delta t)/C_m$, where $\Delta T/\delta t$ are the initial slopes of the plot in Fig. S2(a) [$\Delta T/\delta t$ = 0.27 °C/sec and 0.05 °C/sec for CM and IONP, respectively], C_{water}= 4.2 J/g.K is the specific heat capacity of water, and C_m = 0.02 g/mL is the concentration in iron oxide of the different nanoparticle suspensions. The SARs were estimated as 57 ± 6 W/g_{Fe} and 10 ± 3 W/g_{Fe} for CMs and IONPs, respectively. Therefore, the heating properties of CMs appear far superior to those measured for IONPs.

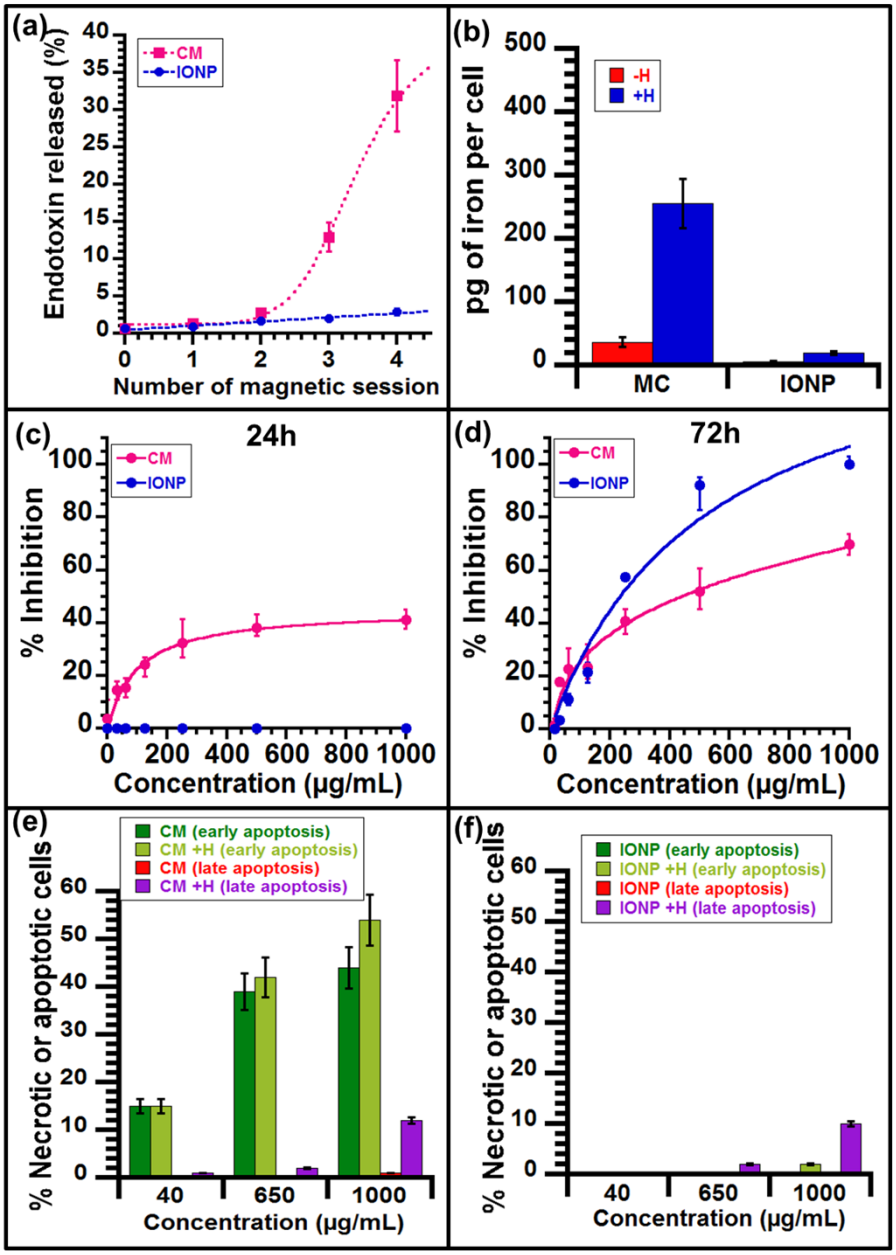


Figure 2: (a) Percentage of endotoxin release from 2 µl suspensions containing 40 µg of CM or IONP in iron oxide that were exposed to 1, 2, 3 or 4 S with an AMF of 198 kHz and average strength of 30 mT applied for 30 minutes. (b) The quantity of iron released from MCs and IONPs, measured in pg and internalized per cell from U87-Luc cells incubated for 24 hours with 1 mg/mL of CM or IONP in maghemite with(+H)/without(-H) AMF, where the AMF is the same as in (a). (c and d) The percentage inhibition of cell proliferation as a function of nanoparticle concentration for CMs and IONPs in maghemite in U87-Luc cells incubated for (c) 24 hours or (d) 72 hours with nanoparticle concentrations varied between 8 µg/mL and 1 mg/mL. (e and f) The percentages of late apoptotic (+ necrotic) and early apoptotic cell death as a function of nanoparticle concentration with(H)/without(-H) AMF where the AMF is the same as in (a) in U87-Luc cells incubated for 24 hours with (e) CM and (f) IONP at concentrations of 40 µg/mL, 650 µg/mL, and 1 mg/mL.

Moreover, the percentage of endotoxin release, which remains relatively similar at 1 to 3% during the first 2 magnetic sessions, strongly increased to 11% and 32% following the third and fourth magnetic sessions, respectively (Fig. 2(a)). This indicates that endotoxins, which are initially at the magnetosome surface, are progressively released from CMs under AMF application. Using CMs exposed to AMF, it therefore appears possible to simultaneously produce heat and release an immune-stimulating substance such as an endotoxin. Although endotoxins cannot be used in medicinal preparations, they may be replaced by a nontoxic equivalent, such as M-PLA, (51), (52). Combining the production of localized heat with the release of such a substance may possibly enhance antitumor efficacy. Compared with CMs, IONPs released a lower quantity of endotoxins and their percentage of endotoxin release did not exceed 5% between 1 and 4 S (Fig. 2(a)). Taken together, these heating and endotoxin release behaviors suggest that IONPs are less promising than CMs for the magnetic hyperthermia and endotoxin treatment in tumors.

3.3. CMs induce enhanced U87-Luc early apoptotic cell death and internalization in vitro

In the absence of the AMF, ***the*** cytotoxicity of CMs towards U87-Luc cells was compared with that of IONPs using nanoparticle suspensions that were added to the cells and incubated for 24 and 72 hours at concentrations between 40 µg/mL and 1 mg/mL. At 24 hours, the percent inhibition of cell proliferation increased with increasing nanoparticle concentrations from 0 to 40% for CM and remained at 0% for the IONPs (Figure 2(c)). At 72 hours, the percent inhibition increased more significantly for CMs, *i.e.,* from

372 0 to 60%, than for IONPs, *i.e.,* from 0 to 100% (Figure 2(d)). While CMs were observed to be more
373 cytotoxic than IONPs at 24 hours, the opposite behavior was observed at 72 hours.
374 U-87-Luc cells were also incubated for 24 hours with CMs and IONPs at three different concentrations
375 of 40, 650, and 1000 µg/ml and then exposed to an AMF of 198 kHz and strength 47 mT for the first 30
376 seconds and 30 mT for the remaining 29.5 minutes in an attempt to reach 41 °C, a temperature above
377 which mild hyperthermia conditions are expected to occur (30). The 40 and 650 µg/ml concentrations
378 led to temperature increases of less than 2 °C, which were insufficient to reach the hyperthermia
379 conditions. These concentrations resulted in necrosis and late apoptosis percentages that remained below
380 ~ 4% with/without AFM for the CMs and IONPs and early apoptosis percentages that were similar
381 with/without AFM at ~ 15% and ~ 40% for CMs at 40 and 650 µg/ml in iron oxide, respectively, and at
382 0% for IONPs (Figs. 2(e) and 2(f)). In contrast, at a concentration of 1 mg/ml, both CMs and IONPs
383 yielded a more significant temperature increase of 7 °C up to 41 °C (Fig. S2(b)), which resulted in an
384 increase in the necrotic and late apoptotic cell death percentages by 10%. These *in vitro* heating
385 behaviors are In contrast, with those observed in solution, where CMs were observed to heat much more
386 than IONPs.
387 The mechanisms of cellular death induced by CMs and IONPs were further examined. CMs appear to
388 induce cellular death mainly through early apoptosis, with a percentage of early apoptotic cell death that
389 increased with increasing CM concentrations from 15% at 40 µg/ml to 50% at 1 mg/ml. Similar
390 percentages were observed for CMs with/without AMF (Fig. 2(e)); this cell death mechanism was not
391 observed with IONPs (Fig. 2(f)).
392 The differences in cell death mechanisms observed for IONPs and CMs as well as the more pronounced
393 decrease in heating efficacy for CMs than IONPs observed between the *in vitro* and in suspension
394 heating conditions may be explained by the different internalization properties. Indeed, the quantity of
395 iron released from the nanoparticles, which are internalized in each cell, increased from 36.8 and 5.5 pg
396 per cell without AMF application to 255.7 and 19.8 pg per cell with AMF application for the CMs and
397 IONPs, respectively. It therefore appears that CMs are internalized better than IONPs and that the

internalization is enhanced by the presence of the AMF for both types of nanoparticles. This enhancement is more pronounced for CMs than for IONP by factors of 7 and 4, respectively (Figure 2(b)). The different internalization properties for the CMs and IONPs may be explained by differences in their charges, *i.e.,* CM and IONP are negatively and positively charged at physiological pH, respectively (Table 1)); differences in organization, *i.e.,* CM and IONP are well-dispersed and tend to aggregate, respectively; and to larger values of coercivity for CMs (200-300 Oe) compared to IONPs (120 Oe) that may enhance CM magnetic field coupling. Furthermore, CM organization in chains may favor internalization by groups containing several magnetosomes (30), *i.e.,* potentially 6 for chains averaging 250 nm in length (Fig. S1(b), while IONPs may result in nanoparticles being internalized one by one or at a lower rate. The enhanced internalization of CMs may favor early apoptosis, which was previously observed with iron oxide nanoparticles, (53), and reduce its heating properties, possibly by preventing nanoparticle Brownian heating mechanisms (54).

3.4. CMs promote enhanced antitumor efficacy towards intracranial U87-Luc glioblastoma

In the *in vivo* studies, mice receive the following treatment at the center of intracranial U87-Luc tumors: (1) glucose followed by treatment or not with magnetic sessions (groups 1 and 2), (2) 40 μg of CMs or IONPs in maghemite without any further treatment (groups 3 and 6), (3) 40 μg of CMs in maghemite followed by 15 magnetic sessions (groups 4 and 5), or (4) 40 μg of IONPs in maghemite followed by 12 magnetic sessions (group 7). The average size of the treated tumors was 3-5 mm^3, except in group 5 where it was 25 mm^3. Following injection, the mice were exposed to 12 to 15 magnetic sessions, during which an AMF of 198 kHz and strength 30 mT was applied for 30 minutes (see Table S1(a) for a summary of the treatment conditions). In this study, U87 cells were labeled with the firefly luciferase gene to evaluate the changes in tumor volumes following the treatments via tumor bioluminescence intensity (BLI) measurements using the relationship between BLI and tumor volumes that we established (Fig. S3) (40), (42), (43), (44). For the mice belonging to the different groups without any measurable production of heat (groups 1, 2, 3, 6, and 7), Figures 3(a) to 3(e) show that the tumor volumes increased following tumor cell implantation without any signs of antitumor activity. Mice

belonging to these groups were rapidly euthanized between days 28 and 42, leading to a rather low median survival time of 42 to 46 days. In contrast, in the mice belonging to groups with heated tumors (groups 4 and 5), antitumor activity is clearly observed and is more pronounced in the small (group 4) than in the large (group 5) treated tumors.

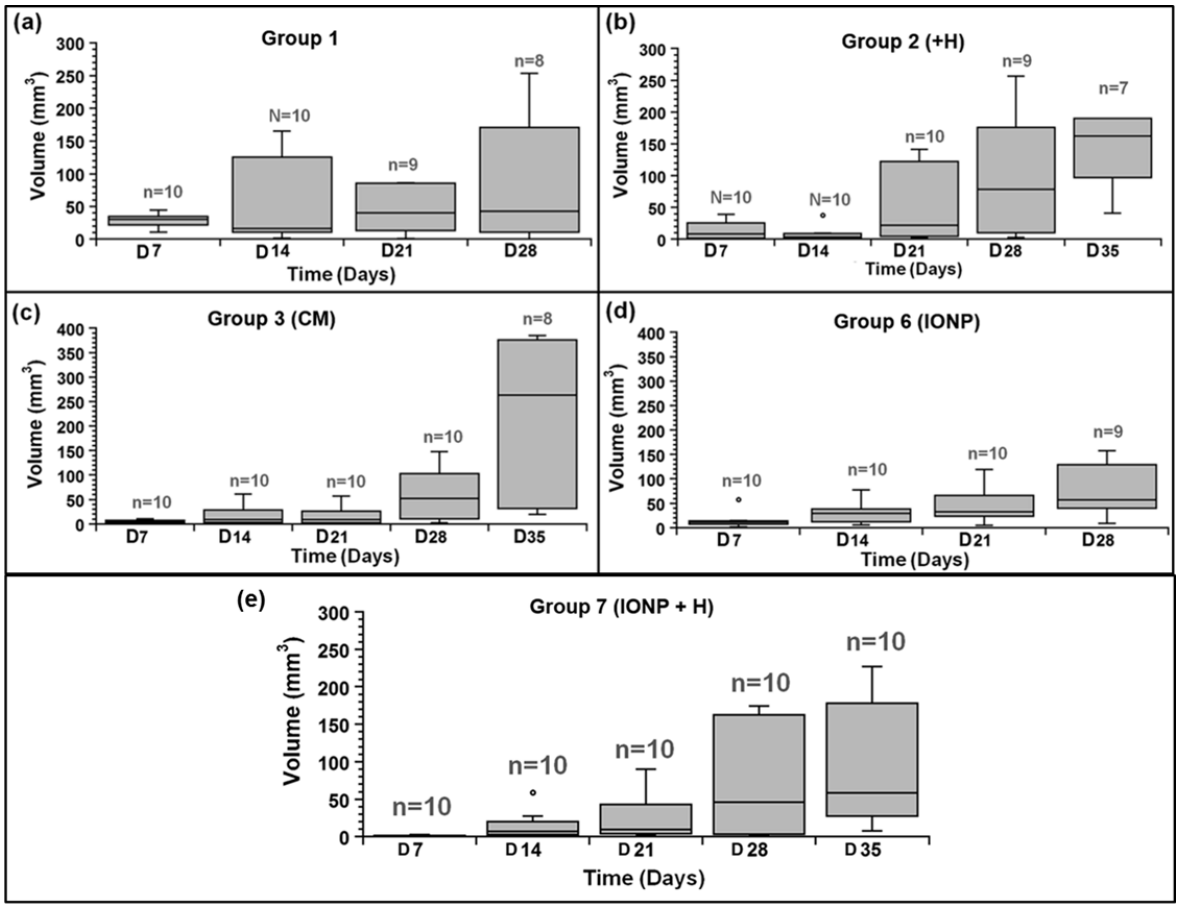


Figure 3: Variations in tumor volumes as a function of time during the days following U87-Luc tumor cell implantation at D0 for (a) untreated mice (group 1), (b) mice exposed to 15 magnetic sessions (group 2, +H), mice receiving a suspension containing either (c) 40 µg of CMs in iron oxide at the site of tumor cell implantation (group 3) or 40 µg of IONPs in iron oxide (group 6, IONP), or (e) 40 µg of IONPs in iron oxide and exposed to 15 magnetic sessions. These variations are plotted using Tukey diagrams, where error bars designate the maximum and minimum tumor volume values, circles represent single tumor values, lower and upper horizontal rectangular sides designate lower and upper quartiles, respectively, and horizontal lines within each box plot represents median tumor volumes. The number of living mice used to draw each box plot (n) is also indicated above each box plot.

Figures 4(a) shows that tumor growth is delayed in group 5 with a median tumor volume that first decreases from 25 mm^3 at day 7 to 5 mm^3 at day 14 and then increases from 5 mm^3 at day 14 to 70 mm^3 at day 42. The behavior of a typical mouse belonging to this group is shown in Figure 4(b), which shows three tumor volume oscillations (decrease followed by increase). This suggests that AMF application causes repetitive anti-tumor activity without preventing tumor regrowth after 15 magnetic sessions. This therapy led to a survival time of 49 days, which is only slightly increased compared to the unheated groups.

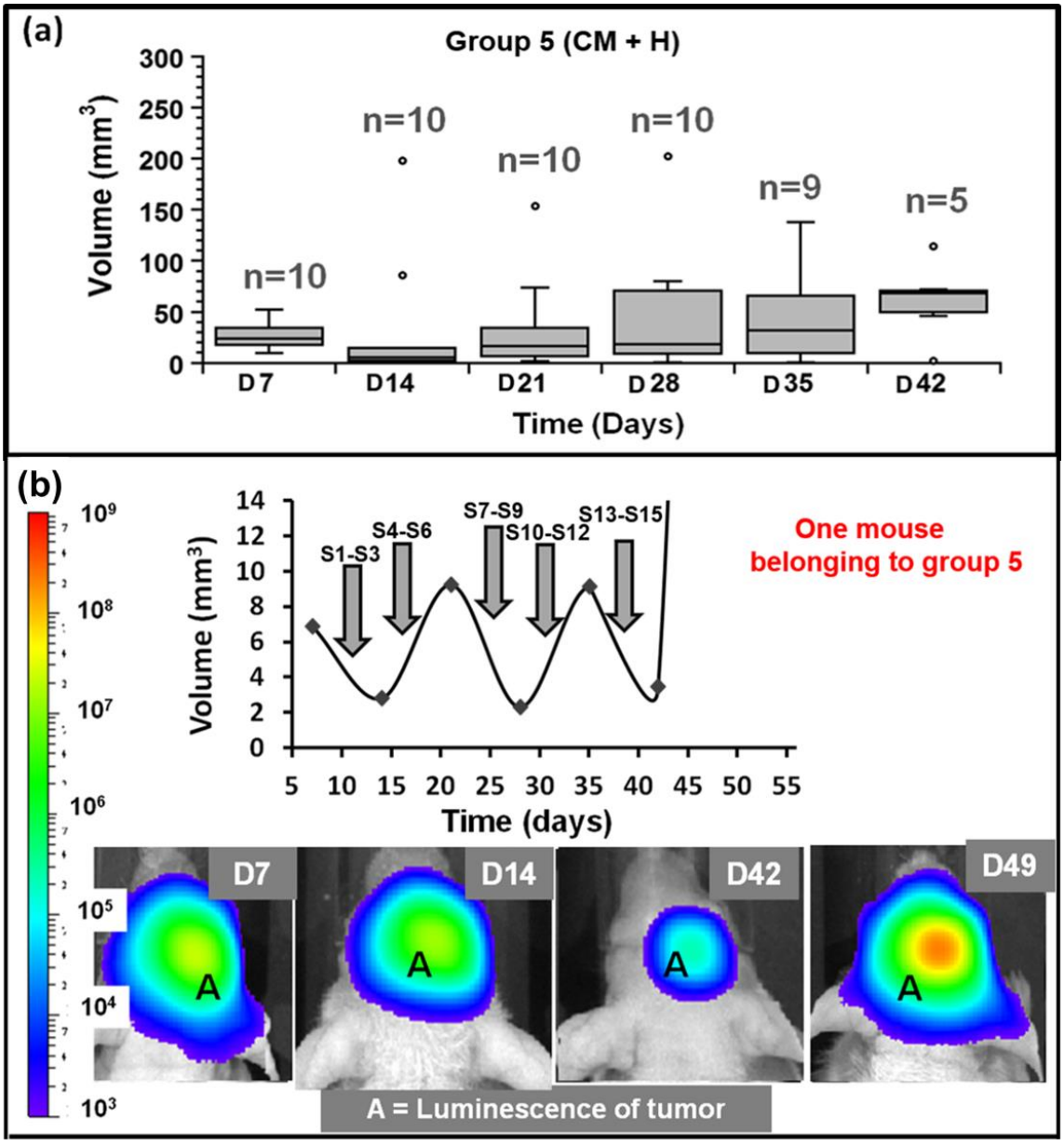


Figure 4: (a) Variations in tumor volumes as a function of time during the days following U87-Luc tumor cell implantation at D0 for mice receiving a suspension containing 40 µg of CMs in iron oxide. The tumors reach an average volume of 25 mm^3 at D7 and were treated with 15 magnetic sessions (group 5, CM+H). (b) Variations in tumor volume and bioluminescence intensity as a function of time during the days following tumor cell implantation in a mouse in group 5 with a tumor volume at D7 of ~7.5 mm^3 that received 40 µg of a suspension of CMs in iron oxide on D7 followed by 15 magnetic sessions (S1 to S15).

Figure 5(a) shows more significant antitumor activity in group 4 with full tumor disappearance at day 35 without tumor regrowth following 1 to 15 magnetic sessions. For a typical mouse belonging to this group, Figure 5(b) shows the gradual decrease in the tumor volume following 1 to 15 magnetic sessions until full tumor disappearance at day 40 without tumor regrowth. Compared with the unheated groups, group 4 had the highest survival at 90 days (p-value < 0.0001).

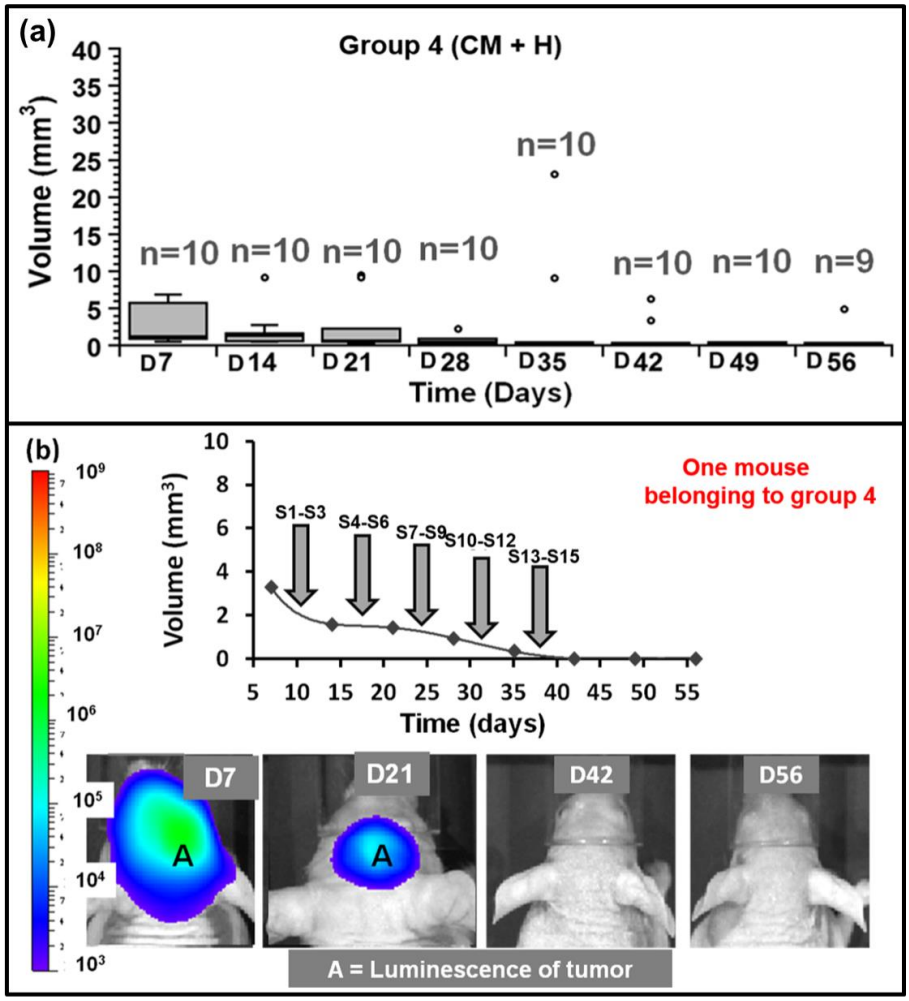


Figure 5: (a) Variations in tumor volumes as a function of time during the days following U87-Luc tumor cell implantation at D0 for mice receiving a suspension containing 40 µg of CMs in iron oxide when the tumors reach an average volume of 3 mm^3 at D7 followed by 15 magnetic sessions (group 4, CM+H). (b) Variations in tumor volume and bioluminescence intensity as a function of time during the days following tumor cell implantation for a mouse belonging to group 4 with a tumor volume at D7 of ~3 mm^3 that receiving 40 µg of CMs in iron oxide on D7 followed by 15 magnetic sessions (S1 to S15).

On day 150, 40% of the mice from this group were still alive without any unusual behaviors. Then, the mice were euthanized and slides of their brains from the tumor cell implantation region were imaged by optical microscopy, revealing the absence of tumors or tumor lesions and a brain neuronal structure identical to that of a healthy brain (Figure 6). These results suggest that the tumors had fully disappeared in these mice. Further analysis of mice from group 4 suggests that treatment does not result in any healthy tissue damage. Indeed, it can be deduced from the optical microscopy images of the brain sections from mice treated with CM with/without AMF collected at different times ranging from 4 hours to 150 days after CM administration (Figs. S4(a) to S4(d), S5(a) to S5(d) and Figs. 8(a) to 8(g), 9(a) to 9(d)) that healthy tissues in the hippocampus and brain do not contain lesions or edema. Such observations can be explained by an LPS-activated neuro-protective response by the microglia (55). Thus, the treatment of the mice in group 4 appears safe and fully efficient.

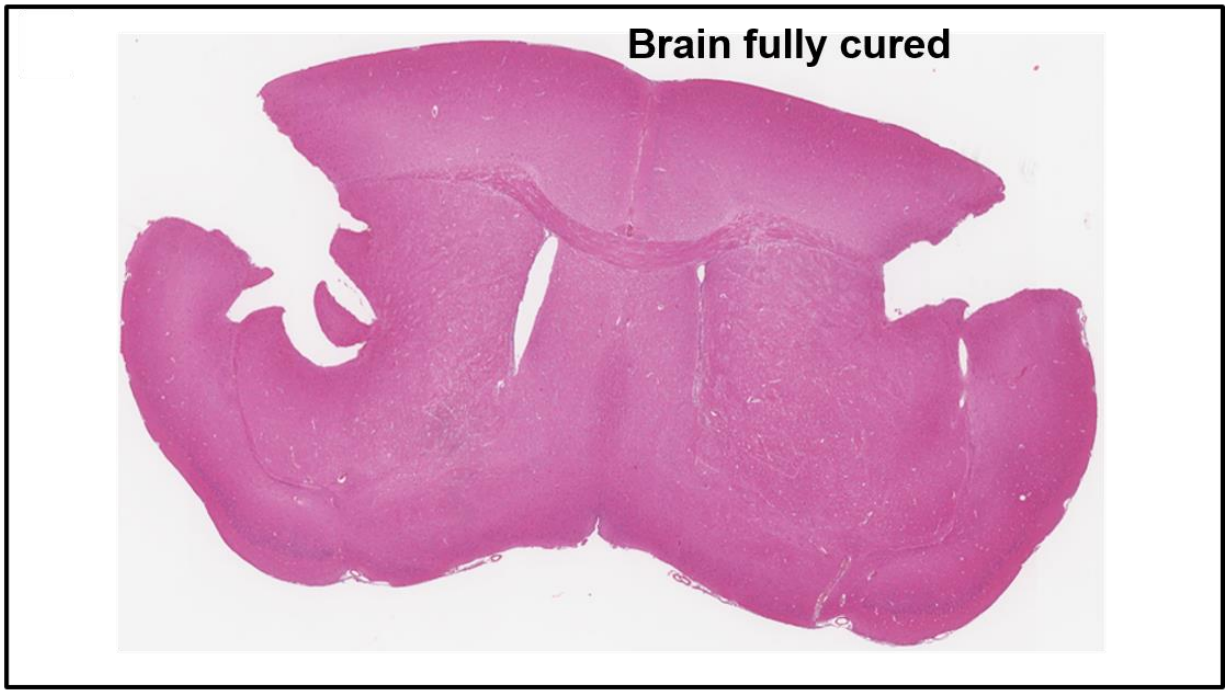


Figure 6: Optical microscopy image of a 4-µm-thick brain section stained with hematoeosin from a mouse in group 4 that received 40 µg of CMs in iron oxide followed by 15 magnetic sessions. This mouse was euthanized 7 months after magnetosome administration. No tumor was observed in this brain section.

3.5. Distribution of CMs in the tumor favors in vivo heating during the various S

CM led to temperature increases of 4 °C at D8 (S1), 1.7 °C at D9 (S2), 0.4 °C at D10, D15 and D16 (S3, S4, S5) and then constant temperatures after D17 (Figures. 7(a) and 7(b)).

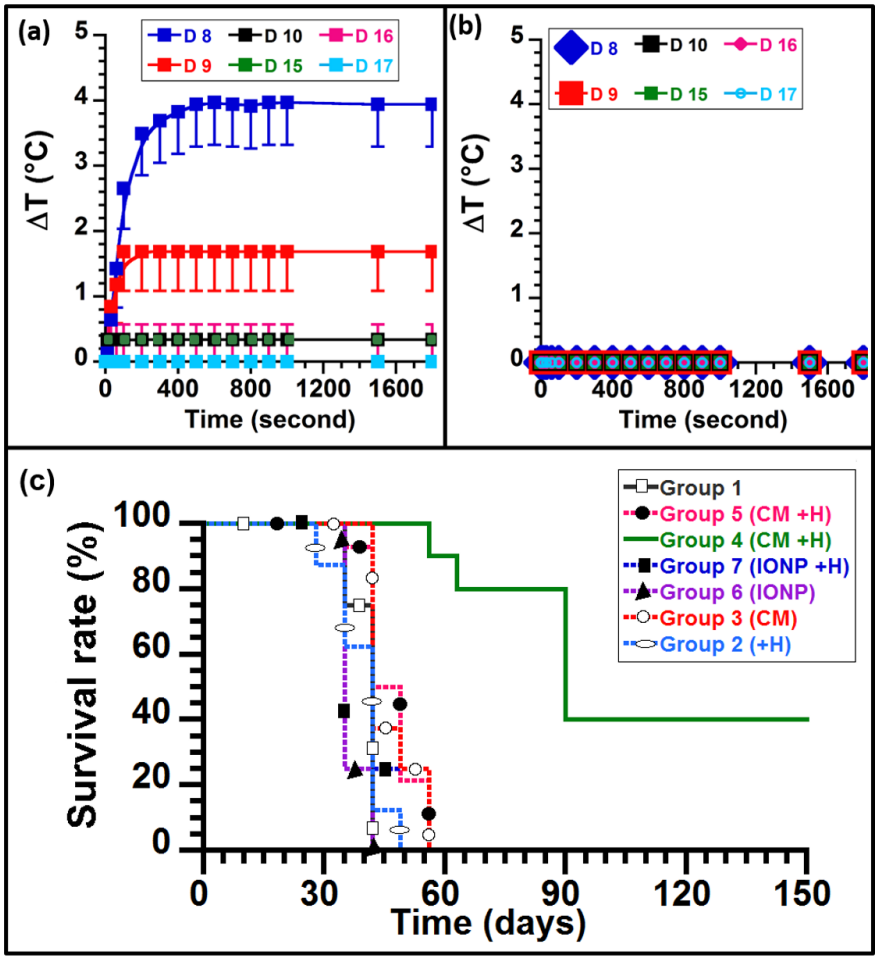


Figure 7: (a), Temperature increases above 28.5 °C observed during each magnetic session (ΔT) on D8, D9, D10, D15, D16 and D17 in the mice from groups 4 and 5 treated with CMs. (b) The same as in (a) for the mice in group 7 treated with IONPs. After D17, tumor temperature increases were no longer observed. (c)Variations in mouse survival times as a function of time during the days following U87-Luc tumor cell implantation for mice with the following treatments: (1) untreated (group 1), (2) exposed to 15 magnetic sessions (group 2), (3) treated with suspensions containing 40 µg of CMs in iron oxide without magnetic sessions (group 3), (4) treated with 40 µg of CMs in iron oxide in ~3 mm^3 tumors followed by 15 magnetic sessions (group 4), (5) administered 40 µg of CMs in iron oxide in ~25 mm^3 tumors followed by 15 magnetic sessions (group 5), (6) administered 40 µg of IONPs in iron oxide (group 6), and administered 40 µg of IONPs in iron oxide followed by 15 magnetic sessions (group 7).

The rather limited increases in temperature under AMF, which are less pronounced than in the capillaries (Fig. S2(a)), may be explained by the effects of AMF on CM distribution. Indeed, the tumor occupation percentage decreases from ~50% right after CM administration without AMF at D8 (Figs. 9(a) and 9(b)) down to 8-15% on D8 and D11 after 1 and 3 magnetic sessions, respectively, (Figs. 8(a),

8(b) and 8(d)). There percentages were estimated by delineating the regions containing the CMs and the tumors and by measuring the ratio between the surfaces of these two regions. Moreover, the decrease in CM heating properties over time may be attributed to internalization of CMs in U87 tumor cells, which was observed at 24 hours after 3 magnetic sessions (Fig 8(d) and 8(e)).

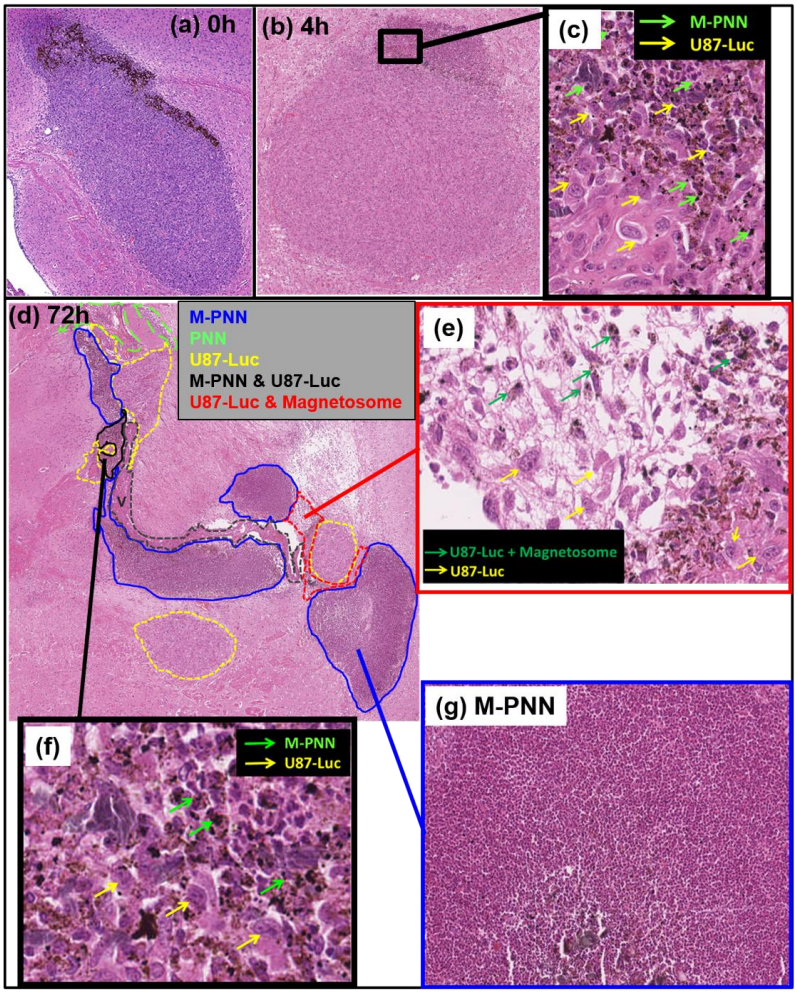


Figure 8: Optical microscopy images of 4 µm thick brain sections stained with hematoeosin from mice receiving 40 µg of CMs in iron oxide and exposed to (a-c) one or (d-g) three magnetic sessions. The mice were euthanized (a) 0 hours (0 h), (b and c) 4 hours (4 h), or (d-g) 72 hours (72 h) after MC administration with either (a-c) one or (d-g) three magnetic sessions. (c) An enlargement of the region in (b). The red arrows in (c) designate polynuclear neutrophils. (e), (f), and (g) are enlargements of three different regions from (d). PNN, M-PNN, U87-Luc, M-PNN & U87-Luc, and U87-Luc & magnetosomes designate polynuclear neutrophils, magnetosomes colocalized with polynuclear neutrophils, U87-Luc cells, magnetosomes colocalized with polynuclear neutrophils and U87-Luc cells, and U87-Luc cells colocalized with magnetosomes, respectively. The regions containing these different cells are surrounded in (d), while individual cells are indicated by arrows in (c), (e) and (f).

In contrast with CMs, IONPs do not produce any heat *in vivo* under the same excitation conditions. This behavior can be explained by their lower concentration in the tumor under AMF applications, *i.e.,* they are observed at the tumor surface as well as part of the tumor periphery at 6 hours (Figs. S4(a) and S4(c)); their more rapid diffusion in the ventricles, *i.e.,* IONPs and CMs localize in the ventricles at 6 and 72 hours, respectively, (Figs. S4(a) and S4(b), Figs. 8(d)); and their earlier internalization in tumor U87-Luc and healthy BETZ brain cells, *i.e.,* IONPs and CMs are internalized at 6 and 72 hours, respectively, (Figs. S4(c) and S4(d), Fig. 8(e)). The combination of a low concentration in the tumor together with rather low SAR may undermine the IONPs' heating power, as was observed *in vivo*.

3.6. CM exposed to AMF activate PNN, which are possibly involved in antitumor activities

Previous studies have reported that immune cells, such as dendritic cells, natural killers, and B and T cells, may participate in tumor destruction following hyperthermia treatment (56). Here, we examined potential involvement of other types of immune cells, *i.e.,* polynuclear neutrophils (PNN), which have only rarely been associated with antitumor activities (57), (58). While PNNs were not detected after glucose (Fig. S5) or IONP (Fig. S4) administration with/without magnetic sessions, we observed that these cells were localized at the same sites as the magnetosomes, forming a complex designated M-PNN in the mouse euthanized 4 hours after CM administration with/without magnetic sessions (Figs. 8(b), 8(c), 8(d), 8(f), 8(g), 9(a) and 9(c)). More precisely, M-PNNs designate assemblies of magnetosomes and PNNs where the magnetosomes are less than 1 μm away from the PNNs. The number of M-PNNs was estimated as 14000-19000 per mm^2 4 hours after CM administration (Table S2). Because PNNs are known to be recruited by endotoxins (59), this behavior could be attributed to the endotoxins surrounding the magnetosome mineral core that attract PNN. Seventy-two hours later, the M-PNNs had disappeared in the absence of AMF (Figs. 9(b) and 9(d) and Table S2) but were detected in large quantities of 27,500 per mm^2 (Table S2) after 3 magnetic sessions either within the tumor periphery (Fig. 8(d) and 8(f)) or in the tumor (Figs. 8(d) and 8(e)).

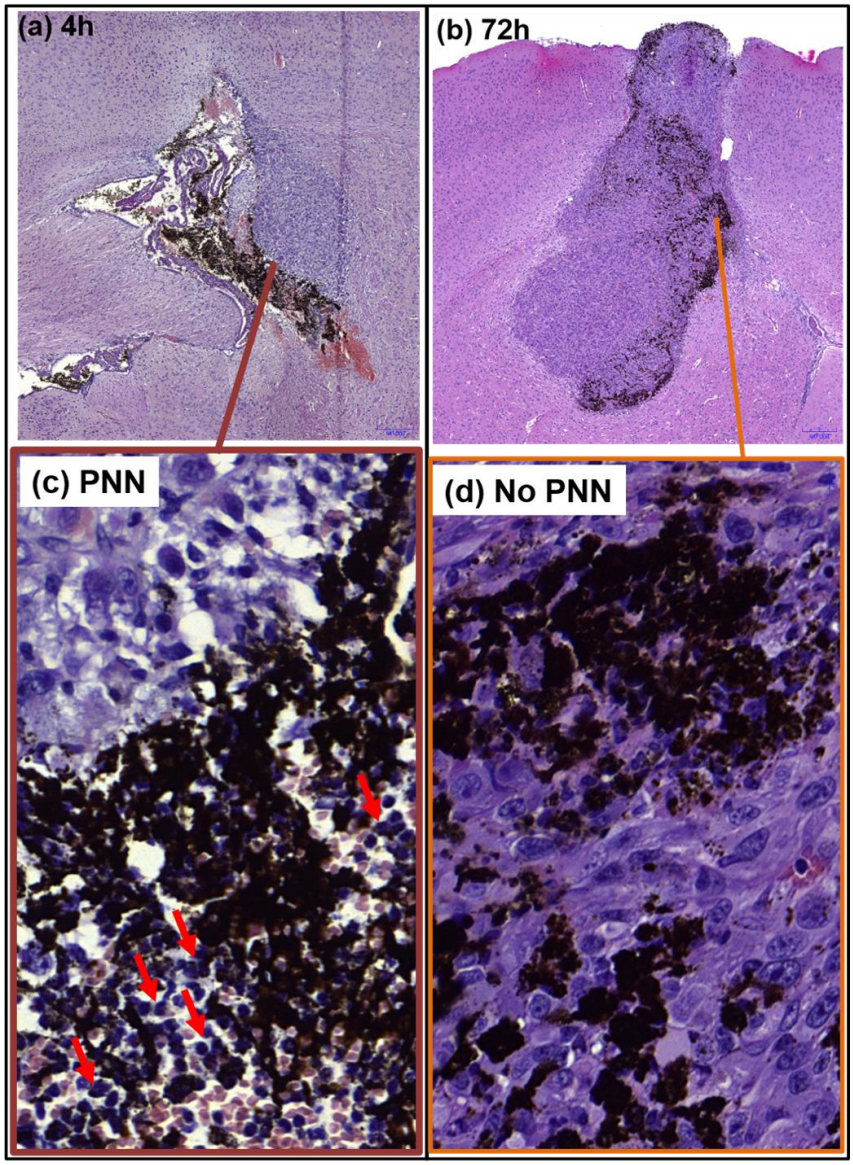


Figure 9: Optical microscopy images of 4 µm thick brain sections stained with hematoeosin from mice receiving 40 µg of CMs in iron oxide without magnetic sessions and euthanized (a) 4 hours (4 h) or (b) 72 hours (72 h) after magnetosome administration. (c) and (d) are enlargements of two regions in (a) and (b), respectively. PNN are observed in (c) and indicated by red arrows, but not in (d).

These interesting behaviors might suggest that in the absence of AMF, endotoxins are progressively deactivated, perhaps due to magnetosome internalization followed by magnetosome and endotoxin decomposition. However, in the presence of AMF, the endotoxins are re-activated, possibly through the release of endotoxins from the magnetosome surface, a behavior that perfectly fits with the observations in solution (Fig. 2(a)) and/or via the destruction of cells in which magnetosomes are initially internalized before AMF application. M-PNN complexes may have two main functions. First, they may be involved

545 in tumor destruction, as they are observed in the tumor region and Toll-like receptor (TLR) from the
546 treated mice could be activated and trigger antitumor activity; this was previously reported for mice
547 bearing B16 tumors (60). Second, they may also be involved in magnetosome capture and re-
548 distribution. Indeed, after one and three magnetic sessions, magnetosomes and PNNs alone are rarely
549 observed in the entire brain, including the tumor regions (Figs. 7(b) and 7(d)), and M-PNNs appear to be
550 located either in the tumor, near the tumor periphery or in the ventricles (Figs. 7(b) and 7(c)). These
551 results suggest that PNNs progressively migrate in the region where the magnetosomes are located
552 between 0 and 4 hours after CM administration to form M-PNN complexes and that these complexes
553 carry the magnetosomes from the inside to the outside of the tumor, possibly through the ventricle blood
554 vessels. This behavior further agrees with the absence of heat production after D17, which suggests that
555 magnetosomes have left the tumor by this date and/or have been dissolved into free iron. This idea is
556 also in line with the well-known function of PNNs, which is to remove bacterial residues (61), (62).
557 Magnetosome progressive departure from the tumor, possibly followed by magnetosome redistribution
558 within the mouse, could be appealing for the treatment by preventing crystallized magnetosomes from
559 remain in the brain for too long a period of time. Optimum treatment conditions correspond to those
560 where magnetosomes remain in the brain long enough to perform the treatment, but not for too long, to
561 avoid unnecessary long-term magnetosome interactions with brain tissues. These conditions may be
562 identified by controlling PNN activation and M-PNN complex formation under AMF application.

563 ***3.7. CMs appear to destroy glioblastoma tumors more efficiently than chemically synthesized***
564 ***nanoparticles under AMF applications***

565 Using the same quantity of nanoparticles administered, we have shown in this study that CMs lead to
566 40% of mice with full tumor disappearance, while IONPs do not yield any observable antitumor
567 activities. This result agrees with previous animal studies performed on mice and rats bearing GBM
568 using intratumor administration of chemically synthesized nanoparticles exposed to AMF that did not
569 improve survival (63) or increased survival by 15 days without resulting in a full cure (64), (26). In
570 addition to being more efficient, magnetosomes could also be used in a lower quantity, thus

571 strengthening treatment safety. Indeed, the quantity of magnetosomes necessary to eradicate U87-Luc
572 GBM in this study, which was 1 to 13 µg in maghemite per mm^3 of tumor volume, is much less than 60
573 µg per mm^3 of tumor volume, which produced less-efficient anti-tumor activities with chemically
574 synthesized nanoparticles (9).

575 **4. CONCLUSION**

576 We demonstrated that 40% of mice bearing intracranial U87-Luc tumors displayed full tumor
577 disappearance after intratumor administration of 40 µg of CMs followed by 12 to 15 magnetic sessions,
578 during which an AMF of average strength 30 mT and frequency 198 kHz was applied for 30 minutes. In
579 contrast, similar antitumor efficacy was not observed when mice were treated with the same conditions
580 and administered chemically synthesized nanoparticles instead of magnetosomes. Furthermore, the
581 absence of mouse brain damage during and following the various treatments appears to indicate that a
582 safe treatment could be performed with magnetosomes, provided that the endotoxins are replaced with
583 an equivalently active but nonpyrogenic substance such as M-PLA. Antitumor activity does not appear
584 to be dominated by nanoparticle cytotoxicity, as the CMs, which are more efficient than IONPs *in vivo*,
585 do not enhance cytotoxicity towards U87-Luc cells compared with IONPs. Moreover, nanoparticle
586 administration without AMF does not produce any observable anti-tumor effects. Instead, tumor
587 destruction appears to be due to the heat produced by the CMs under AMF application, as the only mice
588 that displayed clear anti-tumor effects had their tumors heated (groups 4 and 5). Under heating
589 conditions, tumor tissue destruction may be caused by irreversible cell damage; cytolysis; actin filament,
590 microtubule or mitochondrial dysfunction; DNA replication or RNA synthesis inhibition; or DNA
591 polymerase denaturation (65), but these mechanisms seem insufficient to fully explain the observed
592 antitumor activities. Indeed, tumor destruction does occur when the magnetosomes occupy a small
593 percentage of the total tumor volume (~10%), suggesting that magnetosomes occupying the tumor can
594 induce the destruction of the entire tumor. We have identified the following three possible mechanisms
595 that could be responsible for full tumor destruction:

i) Early apoptosis, as apoptotic cell death is observed to be dominant *in vitro* for CMs and heat was previously shown to favor apoptotic cell death (65), (66), (67);

ii) Microvascular damage due to the presence of magnetosomes in the ventricles that possibly leads to the destruction of the blood vessels supplying the tumor with oxygen, which was previously reported to occur during hyperthermia, (68), and could possibly occur because CMs were observed in the ventricles near the blood vessel; and

iii) the involvement of PNN, which were previously reported to be involved in antitumor activity, (58) and were attracted by the magnetosomes in the tumor region due to the presence of endotoxins at magnetosome surface.

Finally, our study also suggests a method to control magnetosome distribution by attracting PNNs to the magnetosome region, which promotes the formation of magnetosome/PNN complexes that may progressively remove magnetosomes from the tumor through the ventricle blood vessels and enable their elimination. This process appears to be governed by the application (or not) of an AMF.

ACKNOWLEDGMENTS

We would like to thank the Eurostars Program (Nanoneck-2, E9309), subvention AIR from the region of Paris (A1401025Q), the ANRT, the ANR (Méfisto project), the French Research Tax Credit Program, Paris Biotech Santé, BPI, the University Paris 6, the University Paris XI, Marianne Labussière and Elvis Dervishi, as well as all other people and structures in France and Europe that have helped us and been supportive and enthusiastic about our research activities.

Abbreviations

GBM	glioblastoma
AMF	alternating magnetic field
IONP	iron oxide nanoparticles
CM	magnetosome chains

UV	irradiation of an ultraviolet lamp
LAL	limulus amebocyte lysate
DMEM	Dulbecco's Modified Eagle Medium
FBS	fetal bovine serum
HBSS	Hank's Balanced Salt Solution
S	magnetic sessions
BLI	bioluminescence intensity
H&E	hematoxylin-eosin
PNN	polynuclear neutrophils
SAR	specific absorption rates
TLR	toll like receptor
M-PNN	PNN were localized at the same site as magnetosomes

REFERENCES

1. E. Alphandéry, P. Grand-Dewyse, R. Lefèvre, C. Mandawala, M. Durand-Dubief, Cancer therapy using nanoformulated substances: scientific, regulatory and financial aspects. Expert Review of Anticancer Therapy. 15 (2015) 1233–55.

2. D.P. O'Neal, L.R. Hirsch, N.J. Halas, J.D. Payne, J.L. West, Photo-thermal tumor ablation in mice using near infrared-absorbing nanoparticles. Cancer Letters. 209 (2004) 171–6.

3. I.H. El-Sayed, X. Huang, M.A. El-Sayed, Selective laser photo-thermal therapy of epithelial carcinoma using anti-EGFR antibody conjugated gold nanoparticles. Cancer Lett. 239 (2006) 129–35.

4. X.Y. Su, P.D. Liu, H. Wu, N. Gu, Enhancement of radiosensitization by metal-based nanoparticles in cancer radiation therapy. Cancer Biol Med. 11 (2014) 86–91.

5. S. Her, D.A. Jaffray, C. Allen, Gold nanoparticles for applications in cancer radiotherapy: Mechanisms and recent advancements. Advanced Drug Delivery Reviews. (2015) *in Press* http://dx.doi.org/10.1016/j.addr.2015.12.012.

6. O.K. Kosheleva, T.C. Lai, N.G. Chen, M. Hsiao, C.H. Chen, Selective killing of cancer cells by nanoparticle-assisted ultrasound. Journal of Nanobiotechnology. (2016) 14:46.

7. Y. You, Z. Wang, H. Ran, Y. Zheng, D. Wang, J. Xu, and al, Nanoparticle-enhanced synergistic HIFU ablation and transarterial chemoembolization for efficient cancer therapy. Nanoscale 8 (2016) 4324–39.

8. M. Bañobre-López, A. Teijeiro, J. Rivas, Magnetic nanoparticle-based hyperthermia for cancer treatment. Reports of Practical Oncology & Radiotherapy 18 (2013) 397-400.

9. A. Jordan, R. Scholz, K. Maier-Hauff, F.K.H.V. Landeghem, N. Waldoefner, U. Teichgraeber, and al, The effect of thermotherapy using magnetic nanoparticles on rat malignant glioma. J Neurooncol. 78 (2005) 7-14.

10. J.A. Schwartzbaum, J.L. Fisher, K.D. Aldape, M. Wrensch, Epidemiology and molecular pathology of glioma. Nature Clinical Practice Neurology 2 (2006) 494–503.

11. UK CR. Types of primary brain tumors. Last accessed 13 August 2009 at http://www.cancerhelp.org.uk/help/default.asp?page=5014

12. Q.T. Ostrom, L. Bauchet, F.G. Davis, I. Deltour, J.L. Fisher, C.E. Langer, and al, The epidemiology of glioma in adults: a “state of the science” review. Neuro Oncol. 16 (2014) 896–913.

13. R. Stupp, M.E. Hegi, W.P. Mason, M.J. van den Bent, M.J. Taphoorn, R.C. Janzer, and al, Effects of radiotherapy with concomitant and adjuvant temozolomide versus radiotherapy alone on survival in glioblastoma in a randomised phase III study: 5-year analysis of the EORTC-NCIC trial. The Lancet Oncology 10 (2009) 459–66.

14. C. Billecke, S. Finniss, L. Tahash, C. Miller, T. Mikkelsen, N.P. Farrell, and al., Polynuclear platinum anticancer drugs are more potent than cisplatin and induce cell cycle arrest in glioma. Neuro-oncol 8 (2006) 215–26.

15. H.H. Ross, M. Rahman, L.H. Levkoff, S. Millette, T. Martin-Carreras, E.M. Dunbar, and al., Ethynyldeoxyuridine (EdU) suppresses in vitro population expansion and in vivo tumor progression of human glioblastoma cells. J Neurooncol. 105 (2011) 485–98.

16. F-Y. Yang, M-C. Teng, M. Lu, H-F. Liang, Y-R. Lee, C-C. Yen, and al., Treating glioblastoma multiforme with selective high-dose liposomal doxorubicin chemotherapy induced by repeated focused ultrasound. Int J Nanomedicine 7(2012) 965–74.

17. F. Safdie, S. Brandhorst, M. Wei, W. Wang, C. Lee, S. Hwang, and al., Fasting Enhances the Response of Glioma to Chemo- and Radiotherapy. PLOS ONE 7 (2012) e44603.

18. G.L. Bidwell, E. Perkins, J. Hughes, M. Khan, J.R. James, D. Raucher, Thermally Targeted Delivery of a c-Myc Inhibitory Polypeptide Inhibits Tumor Progression and Extends Survival in a Rat Glioma Model. PLOS ONE 8. (2013) e55104.

19. W.L. Titsworth, G.J.A. Murad, B.L. Hoh, M. Rahman, Fighting Fire with Fire: The Revival of Thermotherapy for Gliomas. Anticancer Res. 34 (2014) 565–74.

20. F. Jiang, X. Zhang, S.N. Kalkanis, Z. Zhang, H. Yang, M. Katakowski, and al., Combination Therapy with Antiangiogenic Treatment and Photodynamic Therapy for the Nude Mouse Bearing U87 Glioblastoma. Photochem Photobiol. 84 (2008) 128–37.

21. I. Rabias, D. Tsitrouli, E. Karakosta, T. Kehagias, G. Diamantopoulos, M. Fardis, and al., Rapid magnetic heating treatment by highly charged maghemite nanoparticles on Wistar rats exocranial glioma tumors at microliter volume. Biomicrofluidics. 4 (2010) 024111.

22. M. Shinkai, M. Yanase, M. Suzuki, H. Honda, T. Wakabayashi, J. Yoshida, and al., Intracellular hyperthermia for cancer using magnetite cationic liposomes. Journal of Magnetism and Magnetic Materials. 194 (1999) 176–84.

690 23. A. Ito, M. Shinkai, H. Honda, T. Kobayashi, Heat-inducible TNF-alpha gene therapy combined
691 with hyperthermia using magnetic nanoparticles as a novel tumor-targeted therapy. Cancer Gene Ther. 8
692 (2001) 649–54.

693 24. T. Ohno, T. Wakabayashi, A. Takemura, J. Yoshida, A. Ito, M. Shinkai, and al., Effective
694 Solitary Hyperthermia Treatment of Malignant Glioma Using Stick Type CMC-magnetite. In vivo
695 Study. J Neurooncol. 56 (2002) 233–9.

696 25. B. Le, M. Shinkai, T. Kitade, H. Honda, J. Yoshida, T. Wakabayashi, and al., Preparation of
697 Tumor-Specific Magnetoliposomes and Their Application for Hyperthermia. Journal of Chemical
698 Engineering of Japan. 34 (2001) 66–72.

699 26. K. Maier-Hauff, R. Rothe, R. Scholz, U. Gneveckow, P. Wust, B. Thiesen, and al., Intracranial
700 thermotherapy using magnetic nanoparticles combined with external beam radiotherapy: results of a
701 feasibility study on patients with glioblastoma multiforme. J Neurooncol. 81 (2007) 53–60.

702 27. K. Maier-Hauff, F. Ulrich, D. Nestler, H. Niehoff, P. Wust, B. Thiesen, and al., Efficacy and
703 safety of intratumoral thermotherapy using magnetic iron-oxide nanoparticles combined with external
704 beam radiotherapy on patients with recurrent glioblastoma multiforme. J Neurooncol. 103 (2011) 317–
705 24.

706 28. E. Alphandéry, S. Faure, O. Seksek, F. Guyot, I. Chebbi, Chains of Magnetosomes Extracted
707 from AMB-1 Magnetotactic Bacteria for Application in Alternative Magnetic Field Cancer Therapy.
708 ACS Nano. 5 (2011) 6279–96.

709 29. E. Alphandéry, F. Guyot, I. Chebbi, Preparation of chains of magnetosomes, isolated from
710 Magnetospirillum magneticum strain AMB-1 magnetotactic bacteria, yielding efficient treatment of
711 tumors using magnetic hyperthermia. International Journal of Pharmaceutics. 434 (2012) 444–52.

30. E. Alphandéry, M. Amor, F. Guyot, I. Chebbi, The effect of iron-chelating agents on Magnetospirillum magneticum strain AMB-1: Stimulated growth and magnetosome production and improved magnetosome heating properties. Applied Microbiology and Biotechnology. 96 663–70.

31. E. Alphandéry, S. Faure, L. Raison, E. Duguet, P.A. Howse, D.A. Bazylinski, Heat Production by Bacterial Magnetosomes Exposed to an Oscillating Magnetic Field. J Phys Chem C. 115 (2011) 18–22.

32. E. Alphandéry, I. Chebbi, F. Guyot, M. Durand-Dubief, Use of bacterial magnetosomes in the magnetic hyperthermia treatment of tumours: A review. International Journal of Hyperthermia. 29 (2013) 801–9.

33. E. Alphandéry, Applications of Magnetosomes Synthesized by Magnetotactic Bacteria in Medicine. Front Bioeng Biotechnol. 11 (2014) 2:5.

34. D.E. Bordelon, C. Cornejo, C. Grüttner, F. Westphal, T.L. DeWeese, R. Ivkov, Magnetic nanoparticle heating efficiency reveals magneto-structural differences when characterized with wide ranging and high amplitude alternating magnetic fields. Journal of Applied Physics. 109 (2011) 124904.

35. C. Grüttner, K. Müller, J. Teller, F. Westphal, A. Foreman, R. Ivkov, Synthesis and antibody conjugation of magnetic nanoparticles with improved specific power absorption rates for alternating magnetic field cancer therapy. Journal of Magnetism and Magnetic Materials. 311 (2007) 181–6.

36. K. Cui, X. Xu, H. Zhao, S.T.C. Wong, A quantitative study of factors affecting in vivo bioluminescence imaging. Luminescence. 23 (2008) 292–5.

37. A. Sun, L. Hou, T. Prugpichailers, J. Dunkel, M.A. Kalani, X. Chen, and al., Firefly luciferase-based dynamic bioluminescence imaging: a noninvasive technique to assess tumor angiogenesis. Neurosurgery. 66 (2010) 751–757.

734 38. R. Hashizume, T. Ozawa, E.B. Dinca, A. Banerjee, M.D. Prados, C.D. James, and al., A human
735 brainstem glioma xenograft model enabled for bioluminescence imaging. J Neurooncol. 96 (2010) 151–
736 9.

737 39. E.B. Dinca, J.N. Sarkaria, M.A. Schroeder, B.L. Carlson, R. Voicu, N. Gupta, and al.,
738 Bioluminescence monitoring of intracranial glioblastoma xenograft: response to primary and salvage
739 temozolomide therapy. J Neurosurg. 107 (2007) 610–6.

740 40. O. Szentirmai, C.H. Baker, N. Lin, S. Szucs, M. Takahashi, S. Kiryu, and al., Noninvasive
741 Bioluminescence Imaging of Luciferase Expressing Intracranial U87 Xenografts: Correlation with
742 Magnetic Resonance Imaging Determined Tumor Volume and Longitudinal Use in Assessing Tumor
743 Growth and Antiangiogenic Treatment Effect. Neurosurgery. 58 (2006) 365-372.

744 41. H. Zhou, K. Luby-Phelps, B.E. Mickey, A.A. Habib, R.P. Mason, D. Zhao, Dynamic Near-
745 Infrared Optical Imaging of 2-Deoxyglucose Uptake by Intracranial Glioma of Athymic Mice. PLOS
746 ONE. 4 (2009) e8051.

747 42. D.F. Heitjan, A. Manni, R.J. Santen, Statistical analysis of in vivo tumor growth experiments.
748 Cancer Res. 53 (1993) 6042–50.

749 43. S-J. Kim, H.J. Lee, M.S. Kim, H.J. Choi, J. He, Q. Wu, et al., Macitentan, a Dual Endothelin
750 Receptor Antagonist, in Combination with Temozolomide Leads to Glioblastoma Regression and Long-
751 term Survival in Mice. Clin Cancer Res. 21 (2015) 4630–41.

752 44. E. Alphandéry, A.T. Ngo, C. Lefèvre, I. Lisiecki, L.F. Wu, M.P. Pileni. Difference between the
753 Magnetic Properties of the Magnetotactic Bacteria and Those of the Extracted Magnetosomes: Influence
754 of the Distance between the Chains of Magnetosomes. J Phys Chem C. 112 (2008) 12304–9.

755 45. D.A. Bazylinski, R.B. Frankel, Magnetosome formation in prokaryotes. Nat Rev Micro. 2 (2004)
756 217–30.

757 46. L.C. Branquinho, M.S. Carrião, A.S. Costa, N. Zufelato, M.H. Sousa, R. Miotto, and al., Effect
758 of magnetic dipolar interactions on nanoparticle heating efficiency: Implications for cancer
759 hyperthermia. Scientific Reports. 3 (2013) 2887.

760 47. C. Grüttner, K. Müller, J. Teller, F. Westphal, A. Foreman, R. Ivkov, Synthesis and antibody
761 conjugation of magnetic nanoparticles with improved specific power absorption rates for alternating
762 magnetic field cancer therapy. Journal of Magnetism and Magnetic Materials. 311 (2007) 181–6.

763 48. C.R. Casella, T.C. Mitchell, Putting endotoxin to work for us: monophosphoryl lipid A as a safe
764 and effective vaccine adjuvant. Cell Mol Life Sci. 65 (2008) 3231–40.

765 49. M.E. Astiz, E.C. Rackow, J.G. Still, S.T. Howell, A. Cato, K.B. Von Eschen, and al.,
766 Pretreatment of normal humans with monophosphoryl lipid A induces tolerance to endotoxin: a
767 prospective, double-blind, randomized, controlled trial. Crit Care Med. 23 (1995) 9–17.

768 50. Y. Liu, J. Wang, Effects of DMSA-Coated Fe3O4 Nanoparticles on the Transcription of Genes
769 Related to Iron and Osmosis Homeostasis. Toxicol Sci. 131 (2013) 521–36.

770 51. A. Tomitaka, Y. Takemura, Measurement of Specific Loss Power from Intracellular Magnetic
771 Nanoparticles for Hyperthermia. J Personali NanoMedicine. 1 (2015) 33-37.

772 52. D.A. Bazylinski, R.B. Frankel, Magnetosome formation in prokaryotes. Nat Rev Micro. 2 (2004)
773 217–30.

774 53. M. Creixell, A.C. Bohórquez, M. Torres-Lugo, C. Rinaldi, EGFR-Targeted Magnetic
775 Nanoparticle Heaters Kill Cancer Cells without a Perceptible Temperature Rise. ACS Nano. 5 (2011)
776 7124–9.

777 54. Z. Chen, W. Jalabi, K.B. Shpargel, K.T. Farabaugh, R. Dutta, X. Yin, and al.,
778 Lipopolysaccharide-Induced Microglial Activation and Neuroprotection against Experimental Brain
779 Injury Is Independent of Hematogenous TLR4. J Neurosci. 32 (2012) 11706–15.

55. T. Mentzel, L.F. Brown, H.F. Dvorak, C. Kuhnen, K.J. Stiller, D. Katenkamp, and al., The association between tumor progression and vascularity in myxofibrosarcoma and myxoid/round cell liposarcoma. Virchows Arch. 438 (2001) 13–22.

56. L. Asín, G.F. Goya, A. Tres, M.R. Ibarra, Induced cell toxicity originates dendritic cell death following magnetic hyperthermia treatment. Cell Death Dis. 4 (2013) e596.

57. F. Eriksson, P. Tsagozis, K. Lundberg, R. Parsa, S.M. Mangsbo, M.A.A. Persson, and al., Tumor-Specific Bacteriophages Induce Tumor Destruction through Activation of Tumor-Associated Macrophages. J Immunol. 182 (2009) 3105–11.

58. J. Liang, Y. Piao, L. Holmes, G.N. Fuller, V. Henry, N. Tiao, and al., Neutrophils Promote the Malignant Glioma Phenotype through S100A4. Clinical Cancer Research. 20 (2014) 187–98.

59. A.W. Segal, How Neutrophils Kill Microbes. Annu Rev Immunol. 23 (2005) 197–223.

60. A.C. Silva, T.R. Oliveira, J.B. Mamani, S.M. Malheiros, L. Malavolta, L.F. Pavon, and al., Application of hyperthermia induced by superparamagnetic iron oxide nanoparticles in glioma treatment. Int J Nanomedicine. 6 (2011) 591–603.

61. A. Jordan, R. Scholz, K. Maier-Hauff, F.K.H.V. Landeghem, N. Waldoefner, U. Teichgraeber, and al., The effect of thermotherapy using magnetic nanoparticles on rat malignant glioma. J Neurooncol. 78 (2006) 7–14.

62. K.F. Chu, D.E. Dupuy, Thermal ablation of tumours: biological mechanisms and advances in therapy. Nat Rev Cancer. 14 (2014) 199–208.

63. D.C. Wang, Y. Zhang, H.Y. Chen, X.L. Li, L.J. Qin, Y.J. Li, H.Y. Zhang, S. Wang, Hyperthermia Promotes Apoptosis and Suppresses Invasion in C6 Rat Glioma Cells. Asian Pacific Journal of Cancer Prevention. 13 (2012) 3239–45.

64. A. Morlé, C. Garrido, O. Micheau, Hyperthermia restores apoptosis induced by death receptors through aggregation-induced c-FLIP cytosolic depletion. Cell Death Dis. 6 (2015) e1633.

65. M. Nikfarjam, V. Muralidharan, C. Christophi, Mechanisms of Focal Heat Destruction of Liver Tumors. Journal of Surgical Research. 127 (2005) 208–23.